Acta Geologica Sinica (English Edition), 2019, 93(1): 74–87

The Hizeh-Jan Kaolin Deposit of NW Iran: the Tetrad Effect in REE Distribution Patterns

Ali ABEDINI* and Mansour REZAEI AZIZI

Department of Geology, Faculty of Sciences, Urmia University, 5756151818, Urmia, Iran

Abstract: The Hizeh-Jan kaolin deposit (northwest of Varzeghan, East-Azarbaidjan Province, NW Iran) is a product of the alteration of Eocene andesitic rocks. Based on mineralogical examinations, kaolinite, quartz, smectite, pyrophyllite, muscovite-illite, alunite, calcite, diaspore, goethite and hematite are the most abundant mineral phases in this deposit. The geochemical indicators, such as Y/Ho and Zr/Hf, indicate the non-CHARAC (non-Charge-radius control) behavior of these pairs, which are likely to be due to the occurrence of the tetrad effect phenomenon in this deposit. Simultaneous concave and convex shapes in the chondrite-normalized REE distribution patterns are a remarkable feature of the kaolin samples. Bivariate diagrams of the size of the third tetrad effect (T_3) versus geochemical parameters such as Y/Ho, Nb/Ta and Zr/Hf ratios display two distinct populations for the kaolin samples. The first population is characterized by high T_3 values (>0.13), which are near or on the fault zone. The second population is characterized by low T_3 values (<0.13), and are farther from the fault zone. The obtained results from the geochemical data have furnished compelling evidence that fluid-rock interaction, overprint of hypogene processes by supergene ones, and structural control, are key controlling factors for the occurrence of tetrad effects in REE distribution patterns in the Hizeh-Jan kaolin deposit.

Key words: REE distribution, Tetrad effect, Kaolin, Hizeh-Jan, NW Iran

Citation: Abedini et al., 2019. The Hizeh-Jan Kaolin Deposit of NW Iran: the Tetrad Effect in REE Distribution Patterns. *Acta Geologica Sinica* (English Edition), 93(1): 74–87. DOI: 10.1111/1755-6724.13765

1 Introduction

The gradual increase of the ionization potential of lanthanides due to their contraction causes them to display smooth distribution curves which are controlled by the ionic (CHARAC) behavior of rare earth elements (REE) during geochemical processes in various environments (Bau, 1996). In some cases, normalized REE distribution patterns show irregular curves which comprise 4 groups known as "tetrad-effect" or "Zigzag or kinked curves" which were reported for the first time by Peppard et al. (1969). This phenomenon in the normalized REE distribution patterns is recognized by cusps in the normalized curves which are attributed to ¼, ½, ¾ and complete filling of the *4f* orbital of lanthanides (Jahn et al., 2001). Therefore, evaluation of REE geochemistry and occurrence of the tetrad effect are informative in investigating the genesis of many deposits (Censi et al., 2007; Peretyazhko and Savina, 2010; Feng et al., 2011; Cunha et al., 2012; Nardi et al., 2012; Abedini and Calagari, 2013; Cao et al., 2013; Höhn et al., 2014; Rezaei Azizi et al., 2017; Abedini et al., 2017; Zarei et al., 2017; Abedini et al., 2018a, b).

During recent decades, geochemistry of rare earth elements (REE) has proved to be one of the best tools for understanding the formation mechanism of kaolin deposits, and hence has received worldwide attention from many researchers (e.g. Santos et al., 2006; Kadir and Akbulut, 2009; Baioumy et al., 2012; Baioumy, 2014a, b, c; Kadir et al., 2014; Garcia-Valles et al., 2015; Selmani et al., 2015; Abedini and Calagari, 2015, 2016; Abedini et al., 2016; Dill et al., 2016; Ercan et al., 2016; Tematio et al., 2017). Most kaolin deposits are found near the surface, therefore the formation of these deposits is generally affected by increasing the time, climate, tectonic activities, and biological conditions (Schroeder and Erickson, 2014). These deposits can be divided into two categories: (1) primary deposits which are related to hydrothermal alteration (more common), (2) secondary ones which are the product of residual processes (Abedini and Calagari, 2015).

Kaolin deposits in Iran have been developed during the Precambrian to Miocene in various intrusive to extrusive igneous bodies and carbonate rocks (Ghorbani, 2013). Hence, these deposits in Iran resulting from tectonic and hydrothermal activities are mostly reported in the altered igneous rocks of the Eocene to Oligocene. They are similar to that of most kaolin deposits in Turkey, which can be found in relation to the alteration of andesitic host rocks of the Oligocene to Miocene (Aldanmaz et al., 2000). Except for a few examples, the geochemical factors involved in the distribution, mobilization and differentiation of major and trace elements (including REE) in these deposits have not been investigated in detail.

The Hizeh-Jan kaolin deposit is located ~30 km

* Corresponding author. E-mail: abedini2020@yahoo.com and a.abedini@urmia.ac.ir

http://www.geojournals.cn/dzxbcn/ch/index.aspx
https://onlinelibrary.wiley.com/journal/17556724

northwest of Varzeqan city, East Azarbaidjan Province. This deposit is a typical clayey deposit with an andesitic host rock of Eocene age in NW Iran. No geochemical studies on the Hizeh-Jan kaolin deposit have as yet been undertaken. This study focuses on the REE and Y behavior and the tetrad effects of selected samples from the Hizeh-Jan kaolin deposit to establish the relationships between tetrad effects and a variety of geochemical processes, and use these as geochemical indicators to understand the kaolinization processes. However, in order to clarify the controlling factors of distribution of REE in the deposit, the size of the tetrad effect as a powerful geochemical indicator in the kaolin samples and their correlations with geochemically isovalent pairs such as Zr-Hf, Nb-Ta and Y-Ho were also used.

2 Geological Setting and Geology of the Deposit

Based on the structural classification of Iran (Nabavi, 1976), the Hizeh-Jan kaolin deposit is a part of the Alborz-Azarbaidjan Zone (Fig. 1). This deposit is located in an area with relatively simple geological lithologies, within which 10 separate outcrops cover an area of about 1.5 km^2. The oldest lithologies of the deposit district are agglomerate, volcanic breccia, tuff, trachy-andesite and pyroxene andesite of Eocene age, which cover most parts of this area (Fig. 2). These lithologies are overlain by dacitic tuff, dacite, andesite, quartz monzodiorite and diorite bodies of Oligocene age. The hornblende andesite and trachy-andesite of Pliocene age overlie some parts of the studied district. The youngest lithologies in this area are Quaternary andesite, basalt, agglomerate, lahar and marl (Fig. 2).

Field observations indicate that Eocene andesite rocks in the Hizeh-Jan district were kaolinized through the action of altering solutions. Based on the shape and extent of this deposit, fault-fracture zones near the studied district are a probable mechanism for alteration of host andesitic rocks and formation of the kaolin deposit. Field relationships reveal that faults and fractures as the results of tectonic activities in this district played an important role in controlling ascending hydrothermal fluids that alter the surrounding andesitic rocks. Meanwhile, the massive, white, very soft-powdery and hard, white to reddish are the main features of kaolin outcrops which are observed in the studied district. Therefore, it is obvious that intensity of kaolinization decreases toward proximal and margins.

Irregularly distributed silica lenses within andesitic host rock of the study area are another geological feature in this district. Silica lenses with thicknesses of 0.5 to 3 m cover the kaolin outcrops in some parts. Moreover, Fe-oxides and hydroxides, silicification, gypsum, anhydrite and barite in the form of veins and veinlets are observed within the kaolin occurrences. Also, brecciation and fractures in some parts of the kaolin outcrops were filled by calcites.

3 Sampling and Laboratory Methods

In order to study the major, trace, and rare earth elements distribution in the kaolin deposit and andesitic host rocks (least altered), 12 samples (10 kaolin samples and 2 andesite samples) were systematically taken at 16-30 m intervals along a profile (Fig. 2). Variation in the physical characteristics was the main determining factor

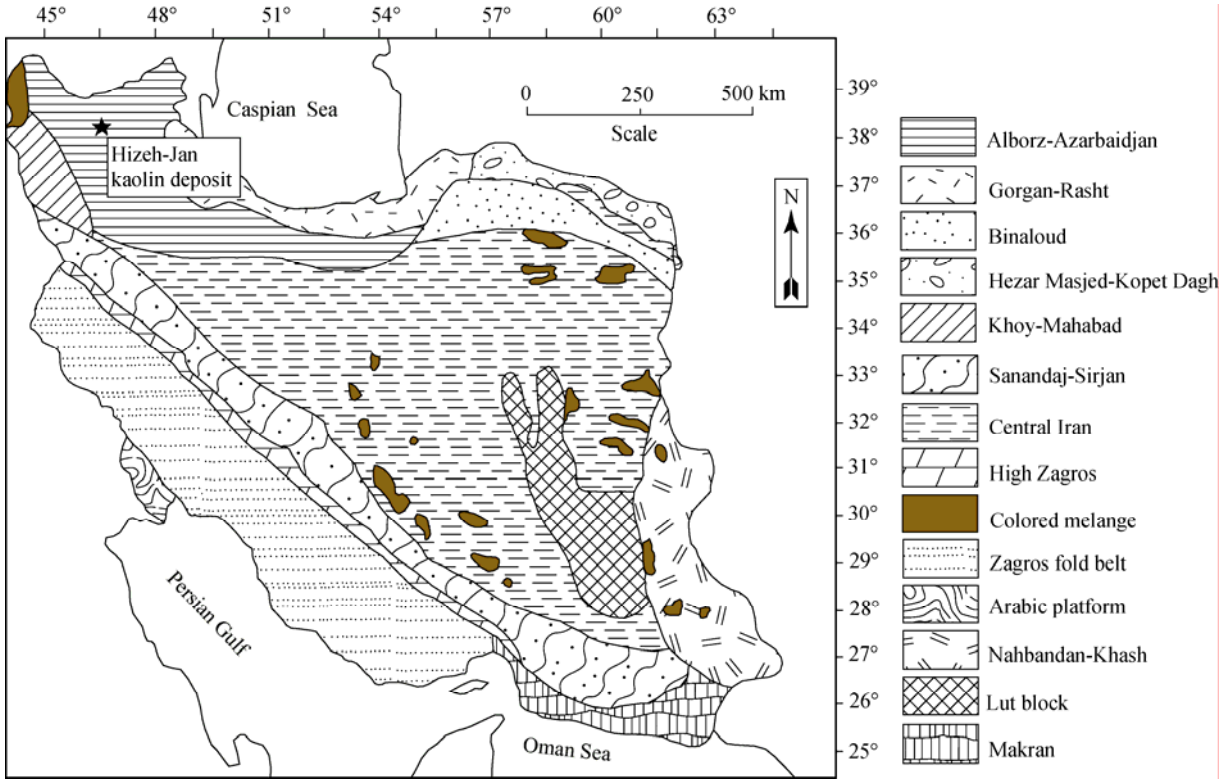

Fig. 1. A simplified map showing the structural zones of Iran (after Nabavi, 1976), in which the location of the Hizeh-Jan kaolin deposit is also shown by asterisk.

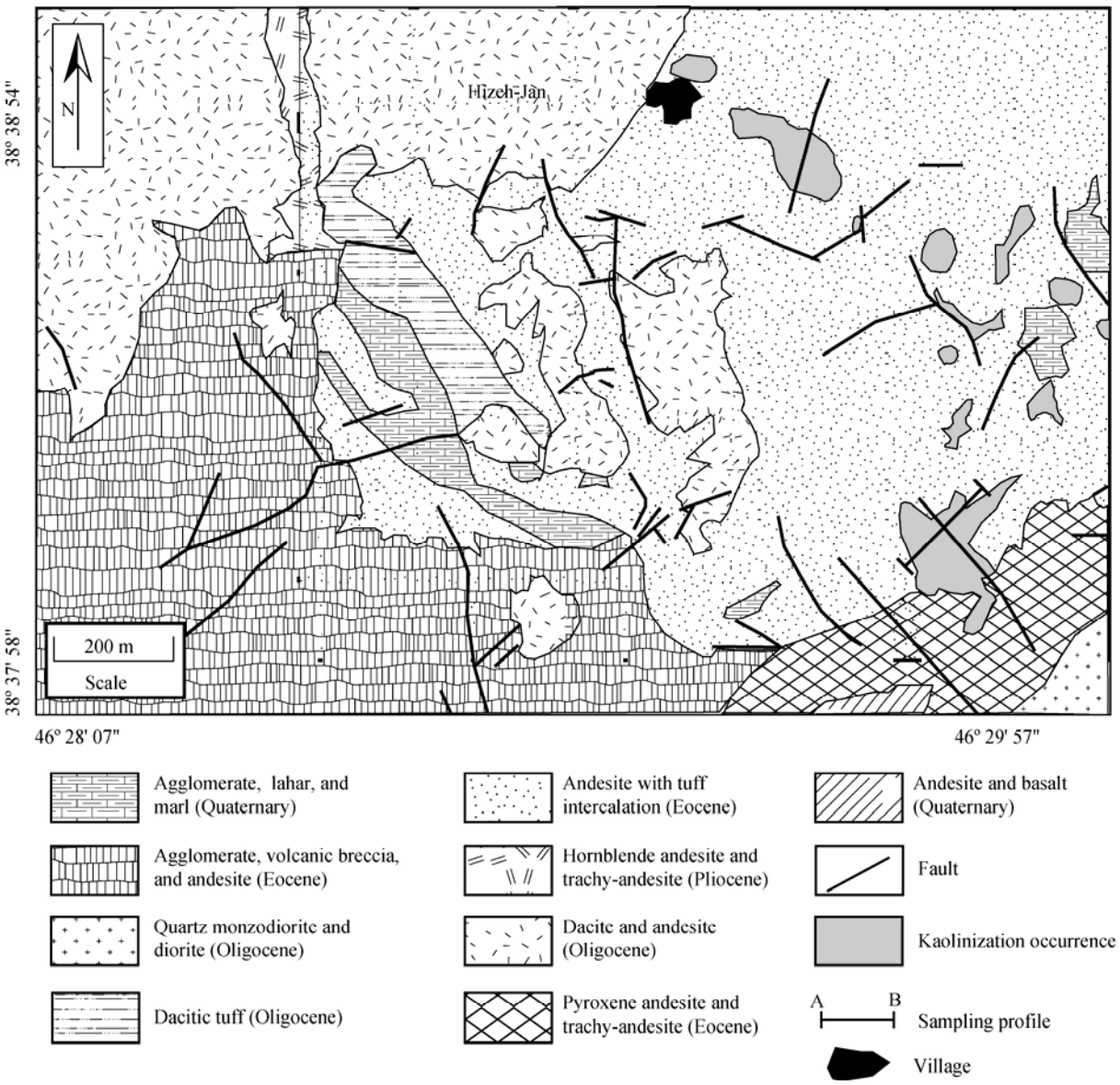

Fig. 2. A simplified geological map of the Hizeh-Jan district.

for sampling from the kaolin deposit. In addition, 10 samples from the andesitic rocks at the contact of the kaolin deposit were also collected. Thin sections from these rocks were prepared and studied under a polarizing microscope.

For determination of unknown mineral phases in the kaolin deposit, 5 samples with different alteration intensities were selected for X-ray diffraction (XRD) analyses using a SIEMENS model D-5000 diffractometer in the Geological Survey of Iran. The XRD analyses were carried out using CuKα radiation, a scanning velocity of 1º 2θ per minute, voltage 40 kV, and beam current 80 mA. The samples were finely ground in an agate mortar and chemically treated with 1 N acetic acid, boiled for 2.5 min in a 0.5 N NaOH solution, and subjected to the sodium dithionite-citrate method (Kunze and Dixon 1986) to remove carbonates, free iron oxides, and amorphous silica. After each chemical treatment, the samples were washed with distilled water. The clay mineralogy was determined by separation of the □2 μm fraction by sedimentation according to Stokes' Law, followed by centrifuge of the suspension at a speed of 5000 rpm for 10 minutes, after overnight dispersion in distilled water. The clay particles were dispersed by ultrasonic vibration for ~15 min. Four oriented specimens of the □2 μm fraction were prepared from each sample, air-dried ethylene-glycol-solvated at 60°C for 2 hours, and thermally treated at 350°C and 550° C for 2 hours. Semi-quantitative relative abundances of rock forming minerals were obtained following Brindley (1980), whereas the abundances of clay mineral fractions were determined using their basal reflections and the intensity factors of Moore and Reynolds (1989).

For determination of chemical composition, andesite and kaolin samples weighing about 3 kg in total were crushed by hand, split into fractions by quartering, and finally ground in a tungsten carbide pestle mortar mill and

sieved to 0.063 mm in preparation for the analytical work. The chemical analyses of all samples were carried out at the ACME Analytical Laboratories Ltd., Vancouver, Canada. The values of the major and trace elements were determined by inductively-coupled plasma emission spectrometry (ICP-ES) and rare earth elements content was determined by inductively-coupled plasma mass spectrometry (ICP-MS) at the same laboratory. The detection limits were between 0.002–0.04 wt%, 0.1–20 ppm, and 0.01–0.3 ppm for major elements (as oxides), trace elements, and rare earth elements, respectively. The values of loss on ignition (LOI) were determined by weight loss of 1 gr. Of sample before and after heating at 950ºC for 90 minutes. Additionally, all the computation, diagrams, and plots were carried out using MATLAB R2012b software.

4 Results

4.1 Mineralogy and petrography

Petrographic examinations revealed that andesitic rocks related to the Hizeh-Jan kaolin deposit have porphyritic texture in the hyalo-microlithic matrix (Fig. 3a), which includes phenocrysts of plagioclase (andesine to labradorite) and ferromagnesian minerals. Phenocrysts of plagioclase are euhedral and tubular crystals and show albite, Carlsbad, and polysynthetic twinnings. Ferromagnesian minerals (hornblende and pyroxene) are seen in the form of anhedral to subhedral crystals in the matrix. Phenocrysts vary from 1 to 4 mm in size. Plagioclases were strongly altered to calcite and in minor amounts to sericite (Fig. 3b). The petrographical studies indicate that accessory minerals such as epidote, apatite, sphene, zircon and opaque minerals such as pyrite, goethite, and hematite can be observed in the matrix of andesite as well. The ferromagnesian minerals in these rocks were partially altered. Some of these minerals were in fine-grain and euhedral form, which were altered to chlorite and Fe-oxides.

The XRD analyses revealed that the Hizeh-Jan kaolin deposit includes kaolinite, pyrophyllite, quartz, smectite, muscovite-illite, hematite, anatase, alunite, diaspore, feldspar, hornblende and calcite (Table 1). Among these, kaolinite is the major mineral phase in the studied samples. Quartz is present as both major and minor mineral phase in the deposit. Smectite, muscovite-illite, hematite, anatase, alunite, diaspore, feldspar, hornblende and calcite are present as minor mineral phases. Pyrophyllite also is the main mineral phase and alunite as a minor mineral phase is observable in the samples of the middle part of the studied profile. Feldspar and hornblende are present in the outer parts of the profile. The presence of pyrophyllite, alunite, and diaspore indicate that the andesitic rocks experienced advanced argillic alteration.

Kaolinite was characterized from diagnostic narrow and sharp peaks at 7.23 and 3.57 Å, with less intense, non-basal reflections including triplets and doublets at 4.46, 4.35, 3.57, 2.49, 2.30 and 1.49 Å which showed well-crystallized kaolinite (Brindley, 1980) (Fig. 4). The basal reflection at 7.23 Å was reduced at 350°C and collapsed at 550° C due to dehydroxylation. These peaks are not affected by ethylene-glycol treatment and suffer a slight reduction following heating to 550° C, due to dehydroxylation. Smectite was determined by a peak at 15.34 Å that expanded to 17.20 Å following ethylene-glycol solvation, and collapsed to 9.90 Å upon heating to 350°C. Further reductions in sharpness and reflection of

Table 1 Mineralogical composition of the kaolin samples of the Hizeh-Jan deposit

	K-1	K-3	K-5	K-7	K-9
Kaolinite	+++	+++	++++	++++	++++
Quartz	++	+	++	++	++
Muscovite-Illite	+	acc	acc	+	
Pyrophyllite		++	++		
Smectite	acc	++	acc		
Hematite	acc	acc	acc	acc	acc
Goethite		acc	acc		acc
Calcite				acc	
Anatase		acc	acc		acc
Diaspore		acc	acc		
Alunite		acc	acc		
Feldspar	+			acc	+
Hornblende	+			acc	+

acc: accessory; +: relative abundance of mineral

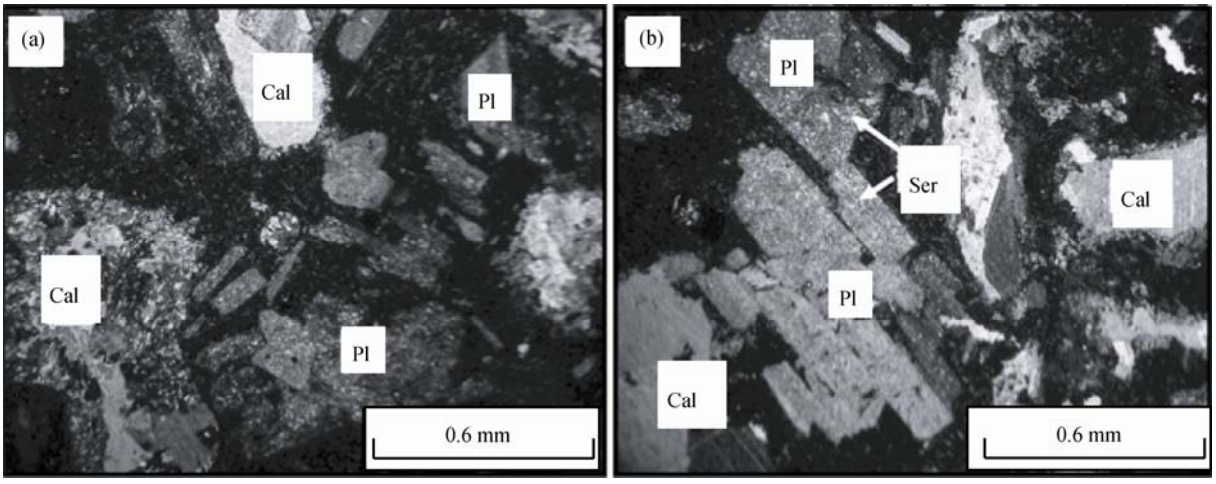

Fig. 3. Photomicrographs of the andesite rocks. (a) Phenocrysts of plagioclase and secondary calcite in the hyalomicrolithic matrix (XPL). (b) Phenocrysts of plagioclase and alteration products such as sericite and calcite (XPL). Abbreviations are: Pl = plagioclase, Cal = calcite, and Ser = sericite.

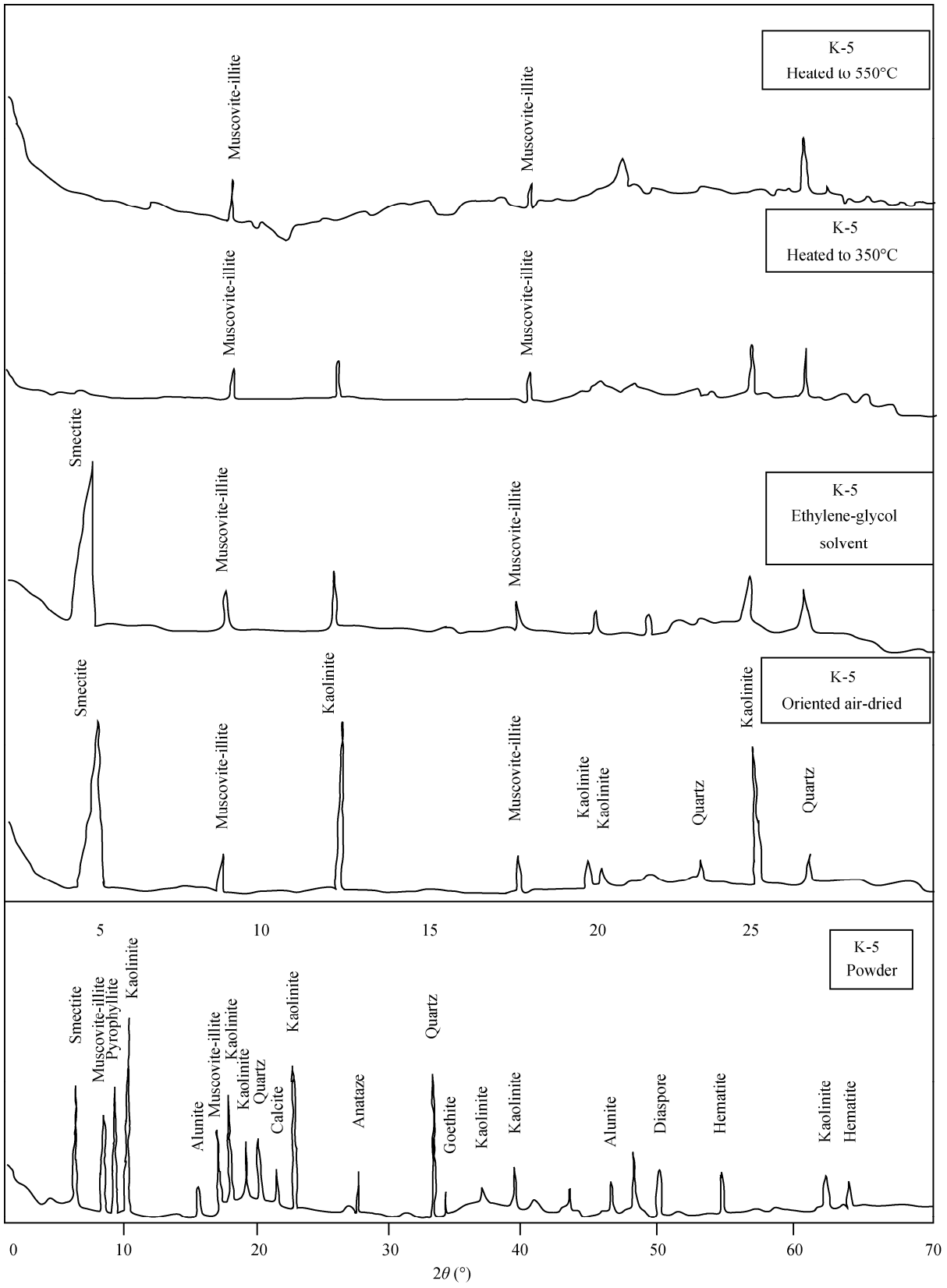

Fig. 4. Pattern of XRD analysis for one typical kaolin sample at Hizeh-Jan.

the peaks were caused by additional heating to 550°C (Fig. 4). Quartz was characterized by reflections at 4.26 and 3.34 Å. Alunite was identified by reflections at 5.73 and 1.90 Å. Muscovite-illite was determined by reflections at 10 and 5 Å. Pyrophyllite and anatase were characterized by peaks at 9.40 and 3.50 Å, respectively. Diaspore, goethite and calcite were indicated by peaks at 1.81, 2.70 and 3.86 Å, respectively. Hematite was characterized by peaks at 1.69 and 1.45 Å (Fig. 4).

4.2 Distribution of major oxides

The results of chemical analyses of the collected samples of the studied district are listed in Table 1. Based on this table, the SiO_2 concentration of the andesite samples display limited variation in the range of 59.25–59.74wt%. The Al_2O_3 and Fe_2O_3 content of the andesite samples display narrow ranges which are between 13.51–14.23wt% and 6.52–6.53wt%, respectively. The concentrations of CaO and Na_2O in the andesite samples are constant, being equal to 5.84wt% and 2.55wt%, respectively. The contents of MgO, K_2O and TiO_2 in the andesites are in the range of 5.31–5.62wt%, 2.89–2.99wt% and 0.62–0.64wt%, respectively. The MnO concentrations of the andesite samples are constant, being equal to 0.09wt%. The contents of Cr_2O_3 and P_2O_5 in the andesite samples display very limited variation in the range of 0.035–0.036wt% and 0.13–0.14wt%, respectively.

The SiO_2 concentration of the kaolin sample in the study area varied between 43.25 and 63.99wt%. The samples in the central part of the studied profile have low SiO_2 concentrations, but the samples towards the margin have higher values. The Al_2O_3 concentration of the kaolin samples increases relative to the andesite samples and varies from 18.45–39.12wt%. In contrast, the content of Fe_2O_3 in the kaolin samples decreased remarkably, varying between 0.13–2.69wt%. The concentration values of CaO and Na_2O in the kaolin samples varied in the range of 0.06–7.12wt% and 0.01–2.91wt%, respectively. The MgO and K_2O concentration of these samples also decreased relative to the andesite samples and varied in the ranges 0.04–2.74wt% and 0.04–2.13wt%, respectively. As the results show, the TiO_2 and MnO concentration display the same decreasing trend in the kaolin samples, relative to the andesite samples. These oxides vary in ranges of 0.16–0.82wt% and 0.01–0.16wt%, respectively. Finally, the Cr_2O_3, and P_2O_5 values in the kaolin samples show variation across 0.009–0.074wt% and 0.06–0.54wt%, respectively.

4.3 Trace element distribution and geochemical ratios

Chemical analyses show the concentrations of Hf, Nb, Ta, Y and Zr in the andesite rocks are in the ranges of 3.5–3.6 ppm, 12.5–13.6 ppm, 0.9–1.2 ppm, 25.4–32.1 ppm and 164.2–165.4 ppm, respectively. By way of contrast, these trace elements in the kaolin samples have ranges of 3.6-5.4 ppm, 4.3–12.1 ppm, 0.3–1.1 ppm, 8.1–20.1 ppm, and 50.4–225.4 ppm, respectively (Table 2).

The SiO_2/Al_2O_3 ratios in the andesite and kaolin samples are in the ranges of 4.16–4.42 and 1.07–3.03, respectively. The Nb/Ta, Y/Ho and Zr/Hf ratios of the andesite samples vary across 11.33–13.89, 32.15–50.16 and 45.61–47.26, respectively. In the kaolin samples the Nb/Ta, Y/Ho and Zr/Hf ratios vary across 4.82–21, 28.21–67.5 and 13.72–57.79, respectively (Table 3).

4.4. REE distribution

The results of the chemical analyses indicate that SREE values of the andesite and kaolin samples are in the ranges of 146.55–162.12 ppm and 39.43–238.4 ppm, respectively (Table 2). The distribution patterns of REE normalized to chondrite (Anders and Grevesse, 1989) display differentiation and enrichment of REE relative to MREE and HREE in the andesite rocks (Fig. 5a) and kaolin samples (Fig. 5b).

The size of Eu/Eu^* and Ce/Ce^* were computed for all samples in this district by using Eq. (1) and Eq. (2) proposed by Bau and Dulsky (1995) and Monecke et al. (2002):

$$Eu/Eu^* = Eu_N/[(Sm_N \times Gd_N)^{0.5}] \quad (1)$$

$$Ce/Ce^* = Ce_N/[(La_N \times Pr_N)^{0.5}] \quad (2)$$

In the above-mentioned equations, N refers to chondrite normalization values from Anders and Grevesse (1989). Table 2 lists the results of Ce and Eu anomaly computations. As illustrated in this table, the computed values for Eu and Ce anomalies in the andesite samples range from 0.97 to 0.98 and 0.92 to 0.99, respectively.

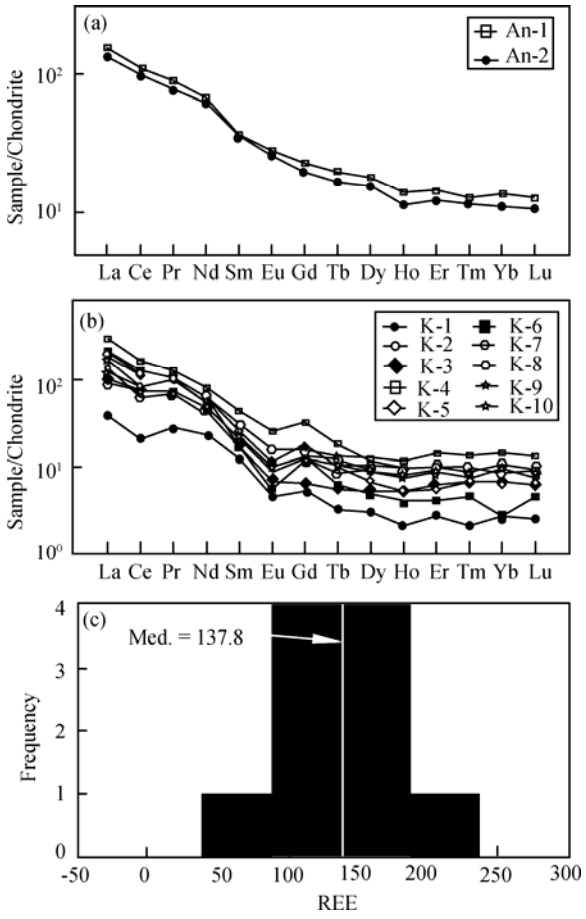

Fig. 5. Chondrite-normalized REE distribution pattern for (a) andesite rocks and (b) kaolin samples. (c) Bivariate frequency diagram against ∑REE values (in ppm) of the kaolin (for details see text).

Table 2 The contents of the major oxides (in wt%), trace, and rare earth elements (in ppm) in the andesite rocks and kaolin samples

		Andesite		Kaolin									
	Detection limit	An-1	An-2	K-1	K-2	K-3	K-4	K-5	K-6	K-7	K-8	K-9	K-10
SiO_2	0.01	59.25	59.74	63.99	62.32	46.52	48.45	41.25	53.98	55.98	60.54	61.87	61.89
Al_2O_3	0.01	14.23	13.51	25.41	24.51	39.12	35.14	38.54	25.68	18.45	20.15	24.45	24.54
Fe_2O_3	0.04	6.52	6.53	0.33	0.83	0.13	0.34	0.33	0.82	2.69	1.32	0.49	0.33
CaO	0.01	5.84	5.84	0.07	0.23	0.12	0.08	0.21	0.06	7.12	0.82	0.13	0.11
Na_2O	0.01	2.55	2.55	0.06	0.28	0.03	0.02	0.02	0.01	0.12	2.91	0.14	0.07
MgO	0.01	5.31	5.62	0.08	0.27	0.09	0.72	2.74	0.04	1.89	0.88	0.15	0.08
K_2O	0.01	2.99	2.89	0.19	2.13	0.12	0.06	0.08	0.04	0.86	0.86	1.07	0.53
TiO_2	0.01	0.62	0.64	0.16	0.82	0.58	0.69	0.53	0.63	0.62	0.51	0.69	0.64
MnO	0.01	0.09	0.09	0.01	0.01	0.02	0.01	0.01	0.01	0.07	0.16	0.01	0.01
Cr_2O_3	0.002	0.036	0.035	0.009	0.039	0.074	0.072	0.064	0.051	0.042	0.053	0.043	0.046
P_2O_5	0.01	0.14	0.13	0.09	0.06	0.32	0.43	0.39	0.54	0.16	0.31	0.13	0.15
TOT/S	0.02	0.04	0.04	0.05	0.04	0.18	0.17	0.17	0.22	0.11	0.08	0.04	0.04
L.O.I.	-	1.72	1.85	9.27	8.45	12.45	13.25	15.21	17.89	11.45	11.18	10.54	11.15
Sum	-	99.346	99.475	99.729	99.999	99.754	99.432	99.544	99.971	99.562	99.773	99.753	99.596
Hf	0.1	3.6	3.5	3.6	5.4	3.7	4.6	3.9	4.1	4.7	4.3	5.1	4.9
Nb	0.1	13.6	12.5	6.3	5.3	10.2	11.5	7.2	4.3	7.3	8.3	11.4	12.1
Ta	0.1	1.2	0.9	0.3	1.1	0.9	0.9	0.7	0.5	0.7	0.9	0.8	0.7
Y	0.1	32.1	25.4	8.1	18.9	12.4	20.1	12.4	9.1	18.5	12.5	19.4	17.5
Zr	0.1	164.2	165.4	50.4	108.6	148.2	165.2	225.4	125.4	64.5	154.2	110.2	160.3
La	0.1	31.2	35.9	9.1	30.4	43.5	69.8	49.8	49.6	38.8	31.2	23.3	32.9
Ce	0.1	60.2	65.1	12.4	39.6	70.4	99.9	76.8	71.3	51.3	48.7	45.2	47.5
Pr	0.02	6.87	7.99	2.39	5.98	10.35	11.25	9.12	10.34	8.88	6.54	6.51	6.65
Nd	0.3	28.4	30.6	10.5	19.2	26.8	35.4	28.4	25.4	25.41	21.2	21.3	20.9
Sm	0.05	5.22	5.44	1.81	2.98	2.33	6.51	4.42	2.51	3.65	3.05	3.01	2.98
Eu	0.02	1.44	1.59	0.26	0.57	0.38	1.52	0.88	0.32	0.62	0.51	0.55	0.52
Gd	0.05	3.89	4.49	1.03	2.61	1.25	6.14	3.31	2.31	3.33	2.52	2.38	2.22
Tb	0.01	0.61	0.71	0.12	0.45	0.21	0.66	0.35	0.22	0.48	0.37	0.39	0.32
Dy	0.05	3.82	4.38	0.73	3.09	1.24	2.91	1.65	1.15	2.74	2.21	2.42	2.11
Ho	0.02	0.64	0.79	0.12	0.67	0.28	0.51	0.29	0.21	0.52	0.42	0.51	0.45
Er	0.03	1.91	2.32	0.43	2.25	0.87	1.59	0.99	0.67	1.47	1.33	1.63	1.39
Tm	0.01	0.28	0.31	0.05	0.33	0.16	0.21	0.17	0.11	0.19	0.22	0.23	0.18
Yb	0.05	1.81	2.19	0.43	2.36	1.11	1.77	1.06	0.43	1.48	1.45	1.78	1.53
Lu	0.01	0.26	0.31	0.06	0.33	0.16	0.23	0.15	0.11	0.18	0.21	0.24	0.22
ΣREE	-	146.55	162.12	39.43	110.82	159.04	238.4	177.39	164.68	139.05	119.93	109.45	119.87

Note: The detection limits for each element are also illustrated. An = andesite sample and K= kaolin sample.

Table 3 Calculated geochemical parameters and tetrad effect values in the andesite rocks and kaolin samples

	Andesite		Kaolin									
	An-1	An-2	K-1	K-2	K-3	K-4	K-5	K-6	K-7	K-8	K-9	K-10
Ce anomaly	0.99	0.92	0.64	0.70	0.80	0.85	0.86	0.75	0.66	0.82	0.88	0.77
Eu anomaly	0.97	0.98	0.58	0.62	0.68	0.73	0.70	0.40	0.54	0.56	0.62	0.61
T_3	0.10	0.06	0.11	0.03	0.05	0.13	0.14	0.20	0.04	0.04	0.02	0.09
T_4	0.00	0.06	0.15	0.04	0.12	0.12	0.10	0.29	0.12	0.06	0.08	0.12
T_t	0.23	0.24	0.36	0.19	0.29	0.35	0.34	0.49	0.28	0.22	0.22	0.33
SiO_2/Al_2O_3	4.16	4.42	2.52	2.54	1.19	1.38	1.07	2.10	3.03	3.00	2.53	2.52
Nb/Ta	11.33	13.89	21.00	4.82	11.33	12.78	10.29	8.60	10.43	9.22	14.25	17.29
Y/Ho	50.16	32.15	67.50	28.21	44.29	39.41	42.76	43.33	35.58	29.76	38.04	38.89
Zr/Hf	45.61	47.26	14.00	20.11	40.05	35.91	57.79	30.59	13.72	35.86	21.61	32.71

Meanwhile, Eu and Ce anomalies of the kaolin samples in the deposit vary across 0.4–0.73 and 0.64–0.88, respectively.

5 Discussion

5.1 Geochemical constraints from trace and rare earth element distributions

Lithophile trace elements such as Y, Zr, Nb, Hf and Ta are used to evaluate geochemical processes during the deposition and evolutionary history of deposits. The trivalent oxidation state and similar atomic radius of Y and Ho cause these two elements to have similar behavior in various geochemical systems (Bolhar et al., 2004). Zr-Hf and Nb-Ta are known as geochemical pairs, also having similar charges and ionic radii, which are used as geochemical indicators to investigate the processes involved during the genesis of deposits. Despite the similar behavior of these geochemical pairs in geological environments, the variations of Y/Ho, Nb/Ta and Zr/Hf ratios (Table 3) are due to different factors such as fluids, solutions, mineral phases, fluid-rock interaction, ligands, complexation and the tetrad effect during the evolution of deposits (Minami et al., 1998; Spandler and Morris, 2016; Rezaei Azizi et al., 2017; Abedini et al., 2018c). Bau (1996) suggested that Y-Ho and Zr-Hf are mostly controlled by their ionic charge and radius (CHARAC) behavior during geochemical processes. The Y/Ho and Zr/Hf ratios of the kaolin samples have superchondritic values and display non-CHARAC behavior, except for sample K-8 (Fig. 6). Based on this figure, the studied samples also display chondritic to superchondritic values

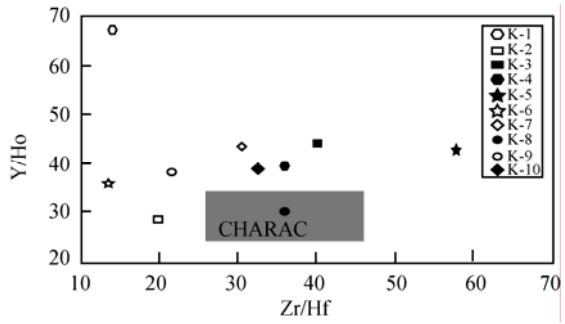

Fig. 6. The diagram of Zr/Hf vs. Y/Ho for studied kaolin samples. The CHARAC field is from Bau (1996).

for Y/Ho ratios and subchondritic to superchondritic values for Zr/Hf ratios.

The chondrite-normalized REE patterns (Fig. 5b) in the kaolin samples reveal enrichment of LREE and depletion of HREE. The frequency diagram of SREE in kaolin samples of the studied district displays variation with a median equal to 137.8 ppm (Fig. 5c). Another observable pronounced phenomenon in Fig. 5b is occurrence of irregular curves known as "zigzag" or "tetrad-effect" in chondrite-normalized REE distribution patterns. The $(La/Lu)_N$ ratio in kaolin samples is considered to be an indicator for determination of the pH of fluids (Kadir and Erkoyun, 2013). $(La/Lu)_N$ ratios higher than 1 indicate a low pH and a low concentration of carbonate, hydroxyls and halogens (Kadir and Erkoyun, 2013). The computed $(La/Lu)_N$ ratio in the kaolin samples of the studied district are in the range of 9.54-46.69. Meanwhile, the developing Fe-oxides (hydroxides) and silicic zones adjacent to the kaolinization areas are indicative of alteration by strongly low pH hydrothermal fluids (Kadir and Akbulut, 2009). On the other hand, the presence of minerals such as quartz, alunite, kaolinite, as well as pyrite in the kaolinized samples is attributed to a pH in the range of 2 to 4 for fluids involved in alteration (Ercan et al., 2016). Moreover, acid sulfate alteration in geological environments is indicative of low pH, high H_2SO_4 concentration, and oxidizing conditions (Rye et al., 1992). Based on the work of these authors, the H_2SO_4 can originate in supergene, steam-heated and magmatic hydrothermal environments, and under supergene conditions, the oxidation of sulfide minerals such as pyrite is the main source for the sulfuric acid.

Among REE, Eu and Ce are oxidation-sensitive elements. Therefore, it can be concluded that Ce and Eu anomalies in a geological environment are strongly affected by the fugacity of oxygen (Ekambaram et al., 1986; Burnham and Berry, 2014; Mondillo et al., 2015). Increasing the oxygen activity in the geochemical process causes trivalent Ce to become less mobile tetravalent Ce (Fulignati et al., 1999; Karakaya, 2009; Abedini and Calagari, 2015). Combining these data and the moderate negative Ce anomaly of the studied kaolin samples, it can be deduced that the kaolinization process of the andesitic rocks is likely to have occurred under relatively oxic conditions. The presence of negative Eu anomalies in the kaolin samples in this deposit are likely due to the intensity of alteration and/or the alteration of mineral phases such as plagioclase in andesites under the higher fugacity of oxygen (Yıldız and Başaran, 2015; Abedini and Calagari, 2015).

Based upon the previously-mentioned hypothesis and the presence of pyrite in the parent rocks, it can be concluded that hydrothermal fluids for the formation of kaolin in this district are likely characterized by a low pH and a relatively high fugacity of oxygen. This hypothesis is completely consistent with the presence of mineral phases such as pyrophyllite and diaspore that are indicative of a magmatic hydrothermal environment (Rye et al., 1992).

5.2 Occurrence of the tetrad effect in kaolin samples

The occurrence of irregular curves in the chondrite-normalized REE distribution patterns of the kaolin samples in the Hizeh-Jan district in the form of both convex (M-shape) and concave (W-type) curves, can be attributed to the impact of the tetrad effect phenomenon on the geochemical processes. In order to quantify the size of the tetrad effects in the chondrite-normalized REE distribution patterns, mathematical methods have been applied (Irber, 1999; Monecke et al., 2002). In this research, the size of the tetrad effects in the chondrite-normalized REE distribution patterns were computed by using Eq. (3) (Monecke et al., 2002):

$$T_i = [0.5\times ([X_{Bi}/(X_{Ai}^2\times X_{Di})^{1/3}-1)]^2+ [X_{Ci}/(X_{Di}^2\times X_{Ai})^{1/3}-1]^2)]\exp(0.5) \quad (3)$$

In this equation, T_i indicates individual tetrads in the chondrite-normalized REE distribution patterns. The size of each tetrad was shown as T_1, T_2, T_3 and T_4 for the 1st, 2nd, 3rd and 4th tetrads, respectively. The concentrations of the first, second, third and fourth elements in each tetrad are labeled as X_{Ai}, X_{Bi}, X_{Ci} and X_{Di}, respectively. The size of T_i indicates the standard deviation of the second and third elements of an individual tetrad from the straight line connecting the first and the fourth elements of the same tetrad. If T_i equals zero, it means that there is no significant tetrad effect. Otherwise, it means that there is a significant tetrad effect in the chondrite-normalized REE patterns. Eq. (3) generates two or three values for tetrads in the chondrite-normalized REE patterns. To quantify the overall T_t values as an average size for tetrads in each chondrite-normalized REE pattern, Eq. (4) can be used (Monecke et al., 2002):

$$T_t= (S([X_{Bi}/(X_{Ai}^2\times X_{Di})^{1/3}-1]^2+ [X_{Ci}/(X_{Di}^2\times X_{Ai})^{1/3}-1]^2)/2N)\exp(0.5) \quad (4)$$

where X_{Ai}, X_{Bi}, X_{Ci}, and X_{Di} are the same as Eq. 3. The average values of T_t should be calculated for all available tetrads (1st, 3rd, and 4th tetrads). The first tetrad will be ignored, if Ce displays anomalous behavior. T_t values greater than 0.2 are indicative of a significant tetrad effect phenomenon in the chondrite-normalized REE distribution pattern (Monecke et al., 2002).

The computed sizes of tetrad effects in the kaolin and andesite samples of the studied district are listed in Table 3 and displayed in Fig. 7a–d. The size of the T_3 tetrad effect of the andesite and kaolin samples are in the ranges of 0.06–0.1 and 0.02–0.2, respectively. Meanwhile, the size of the T_4 tetrad effect of the andesite and kaolin

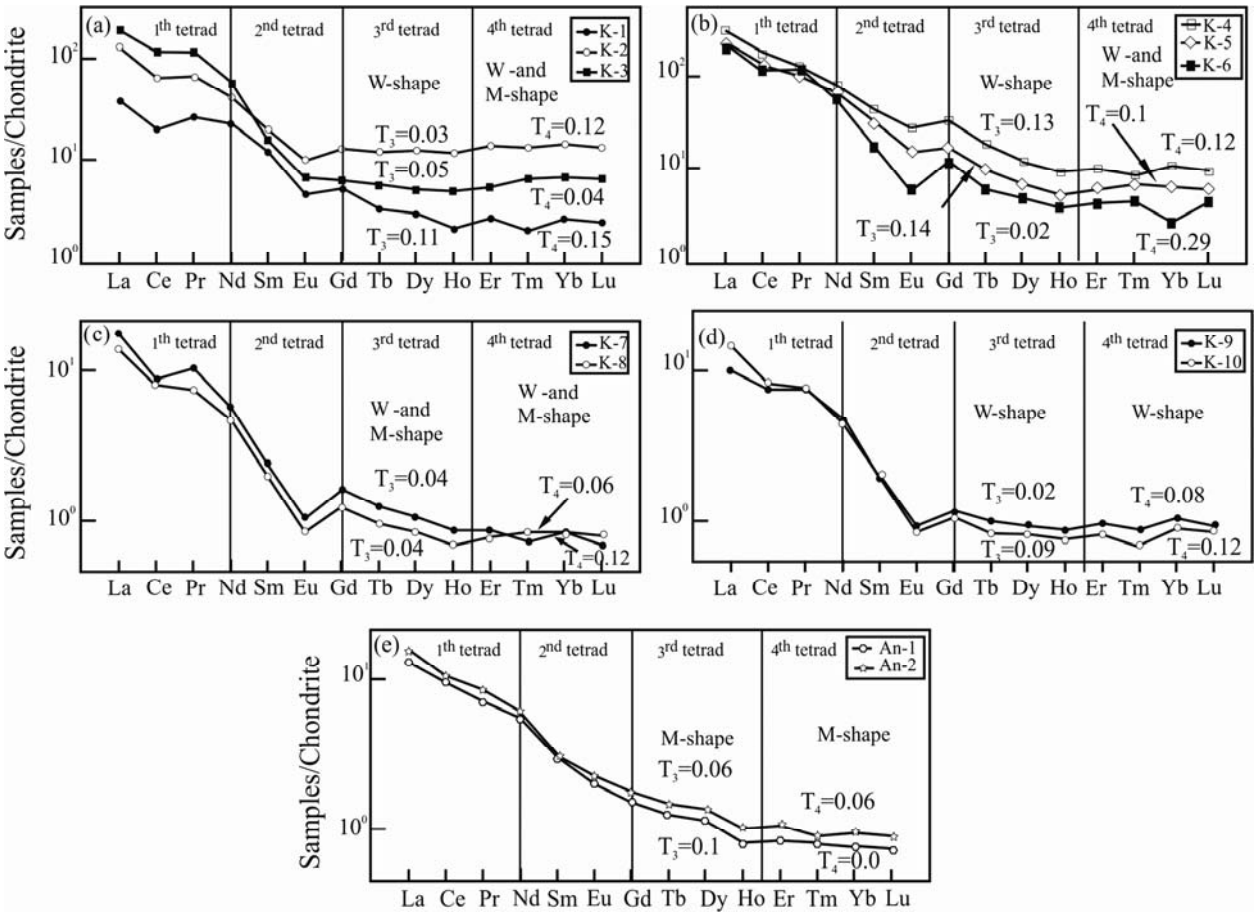

Fig. 7. Chondrite-normalized REE diagrams for kaolin samples (a-d) and andesite rocks (e). The size of T_3 and T_4 are the first, third, and fourth tetrads, respectively, and are calculated following Monecke et al. (2002). Chondrite values are from Anders and Grevesse (1989).

samples are in the ranges of 0.00–0.06 and 0.04–0.29, respectively. The chondrite-normalized REE patterns of the andesite samples in this district display the M-shape tetrad effect phenomenon (Fig. 7e), which is characteristic of igneous systems. The kaolin samples of this area present significant contemporaneous concave (W-shape) and convex (M-shape) tetrad effect phenomena both in the third and fourth tetrads (Fig. 7a–d). The sizes of the T_3 tetrad effect vary in a narrow range relative to the T_4 values. Therefore, in this research, the calculated sizes of the T_3 (third) tetrad effect were used to evaluate the geochemical processes.

Mathematical methods such as statistical analysis are generally a preferred method for investigating the geochemical characteristics involved in study areas and facilitating modeling and/or simulation of deposition paleo -conditions and environments (Wang et al., 2017). Based on the frequency diagram of the T_3 tetrad effects for all samples of the studied district, it is clear that the distribution pattern of the computed T_3 tetrad effect values present a substantial bimodal pattern (Fig. 8a), which can be due to various geochemical conditions and/or the geological environment during deposition (Badel et al., 2011). The clusters of the samples in this district were classified on the basis of the geological relationships, spatial distribution and field observations (Fig. 8a and b). As these figures illustrate, two distinct separate populations are distinguishable in this geochemical system. The first population includes kaolin samples with very low T_3 tetrad effect values with a median equal to 0.04 (Fig. 8b). In contrast, the second population includes kaolin samples which have remarkable T_3 tetrad effect values with a median equal to 0.13 (Fig. 8c).

A bivariate diagram of the computed sizes of the T_3 tetrad effect versus the T_4 tetrad effect indicates two generations for the studied samples (Fig. 9). The field observations reveal that the first population, pertaining to low T_3 tetrad effect values (Fig. 9), are the kaolin samples far from the fault zone. In contrast, kaolin samples which were collected near the fault zone of this district display pronounced greater T_3 tetrad effect values (second population in Fig. 9). This figure indicates that kaolin samples near the fault zone present remarkable T_3 tetrad effect values. This means that T_3 tetrad effect values of kaolin samples can be used as a good geochemical indicator to distinguish the fault zone in this type of deposit.

The diagrams of the size of the T_3 tetrad effect versus the Ce and Eu anomaly for all kaolin samples in the studied district were plotted (Fig.10a–b). As shown in this

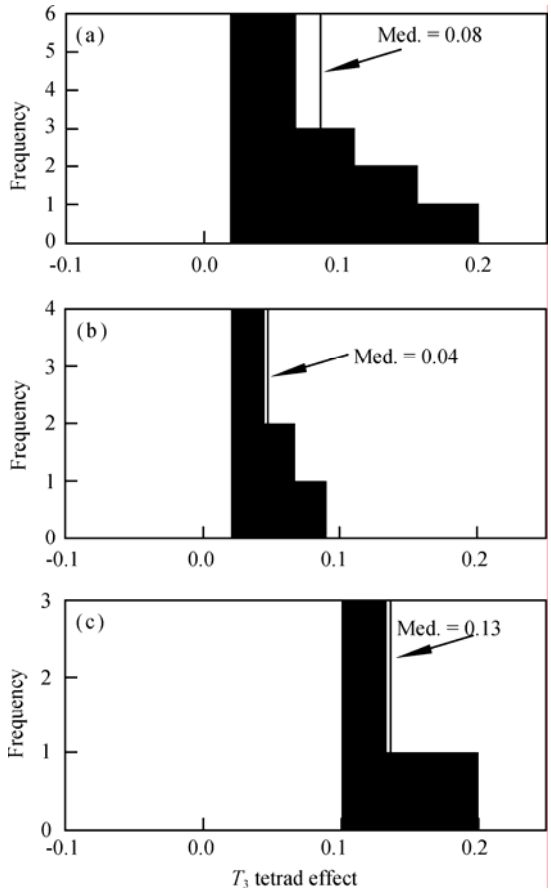

Fig. 8. (a) Frequency diagram of the kaolin samples vs. the computed T_3 tetrad effects. (b) The 1st population of the T_3 tetrad effects with a median of 0.04 for the kaolin samples. (c) The 2nd population of the T_3 tetrad effects with a median of 0.13 for the kaolin samples.

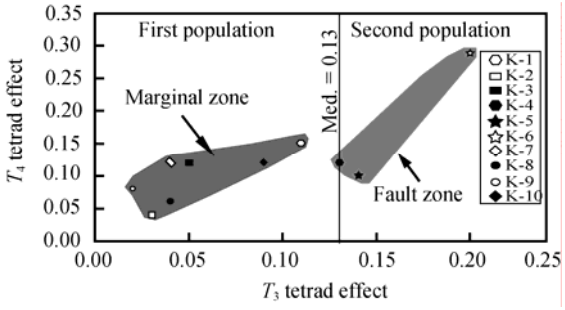

Fig. 9. Plots of the T_3 tetrad effect values vs. T_4 tetrad effect values in the kaolin samples, showing fault zone and marginal zone of the studied district.

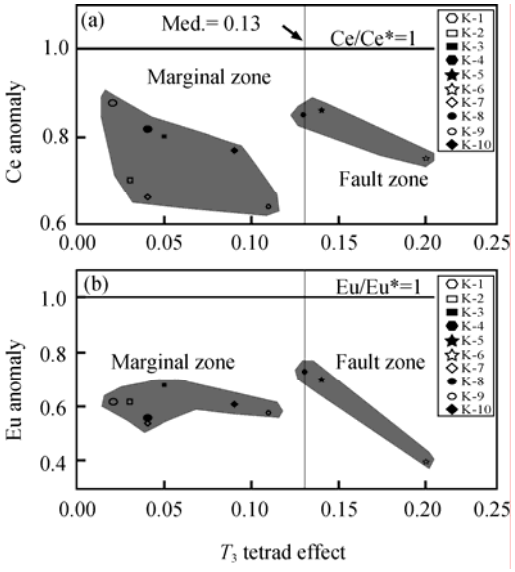

Fig. 10. Diagram of the T_3 tetrad effect values of the kaolin samples versus (a) Ce anomaly and (b) Eu anomaly.

figure, two distinct groups of samples can be observed in the figure, which may be due to different stages, composition, and/or temperature of the hydrothermal fluids during alteration of the andesite rocks. The first population includes the kaolin samples (K-1, K-2, K-3, K-7, K-8, K-9, and K-10) with moderate negative Ce and Eu anomalies and low T_3 tetrad effect values (<0.13). In contrast, the second one includes kaolin samples (K-4, K-5, and K-6) with a similar negative Ce and Eu anomalies trend and greater T_3 tetrad effect values (>0.13). Moreover, the presence of moderate negative Ce anomalies in the kaolin samples can be due to decomposition of minerals such as zircon under low pH and oxic conditions (Fulignati et al., 1999). Consequently, the presence of moderate to relatively strong Eu anomalies and a M-shape tetrad effect phenomenon with remarkably high values in the kaolin samples (K-4, K-5, and K-6) near the fault zone of the studied district support this idea that hypogene hydrothermal fluids, a low pH, and a relatively high fugacity of oxygen were likely the main alteration fluids in this district. Furthermore, it can be concluded that tectonics played an important role during the development of the studied kaolin deposit.

5.3 Correlation between the T_3 tetrad effect, Nb/Ta, Y/Ho and Zr/Hf ratios

During the hydrothermal evolution of a system, geochemical pairs such as Nb-Ta, Zr-Hf and Y-Ho are fractionated and display non-CHARAC behavior (Bau, 1996; Irber, 1999). The non-CHARAC behavior of geochemically isovalent pairs during the evolution of a system can reflect the various depositional conditions. Graphically, the non-CHARAC behavior of these geochemically isovalent pairs versus the computed size of the T_3 tetrad effect can be helpful to interpret and better understand the geochemical processes of the system (Fig. 11a–c).

Previous studies have shown that fractionation between Zr and Hf can be due to geochemical factors such as crystallization, hydrothermal origin of the fluids, metamorphism, and the occurrence of the tetrad effect in geochemical systems (Tang et al., 2014; Rezaei Azizi et al., 2017). Geochemical investigations indicate that there are two separate populations within the kaolin samples, which display both superchondritic and subchondritic Zr/Hf ratios (Fig. 11a). The first population includes the

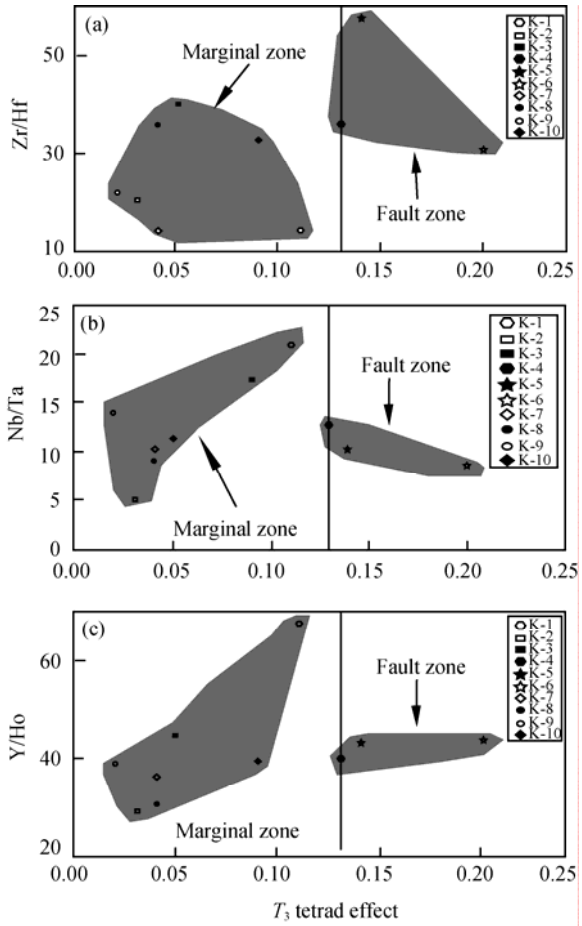

Fig. 11. The diagram of the third tetrad effect (T_3) values of the kaolin samples versus (a) Zr/Hf, (b) Nb/Ta, and (c) Y/Ho ratios. Dashed line indicates the median = 0.13.

kaolin samples with high T_3 tetrad effect values (>0.13), which are indicative of a fault zone in the studied district. The second population includes the kaolin samples with very low T_3 tetrad effect values (<0.13), which are far from the fault zone.

Nb and Ta as geochemical twins are geochemically similar pairs which are characterized by the same ionic charge and radius (Ballouard et al., 2016). Nevertheless, fractionation between these two elements is due to increasing the solubility of these pairs with temperature in F-rich fluids, a reducing environment, and decomposition of biotite (Zaraisky et al., 2010; Stepanov et al., 2014; Dostal et al., 2015). Based on the calculated results (Fig. 11b), it is clear that all kaolin samples (except K-2) in the Hizeh-Jan have Nb/Ta ratios greater than 5 (chondritic ratio). Meanwhile, the Nb/Ta ratios of all samples (except K-2 with its Nb/Ta ratio=4.82) are in the narrow range of 8.6–21. These narrow and relatively low ratios indicate that the hypogene hydrothermal fluid(s) had a moderate temperature. Based upon this data, it can be deduced that hypogene fluids are likely to have altered the andesite rocks in the Hizeh-Jan district.

Geochemical studies proved that fractionation of Y from Ho and existence of both W- and M-shape tetrad effects in the chondrite-normalized REE patterns of a geochemical system reflect the role of fluids and/or solutions during the evolution of that system (Minami et al., 1998). As the plotted diagram shows, the studied kaolin samples in this district represent two different generations of Y/Ho ratios (Fig. 11c). The first generation includes kaolin samples with higher Y/Ho ratios and greater T_3 tetrad effect values (>0.13). These groups of kaolin samples are near the fault zone and reflect the role of the fault as the main conduit (Ercan et al., 2016) for uprising hydrothermal fluids during alteration of the precursor rocks. The second generation of samples includes the kaolin samples with lower Y/Ho ratios and T_3 tetrad effect values, which are farther from the fault zone in this district. Thus, it can be deduced that medium temperature hydrothermal fluid(s) were likely responsible for the alteration of andesitic precursor rocks.

5.4 Main causes for the tetrad effect phenomenon

The presence of concave (W-shape), convex (M-shape), and in some cases simultaneous concave and convex tetrad effects in the chondrite-normalized REE patterns reflect the physico-chemical conditions and/or geochemical parameters during deposition and/or later processes such as hypogene alteration and supergene weathering (Takahashi et al., 2002; Zhao et al., 2002; Monecke et al., 2007; Badanina et al., 2010; Wu et al., 2011; Cao et al., 2013). Generally, igneous rocks and systems during crystallization and the interaction of hydrothermal fluids with wall rocks under alteration processes present a convex (M-shape) tetrad effect in chondrite-normalized REE patterns (McLennan, 1994; Monecke et al., 2007; Rezaei Azizi et al., 2017). These scenarios support the idea that crystallizations of mineral phases (McLennan, 1994) in magmatic and/or hydrothermal systems can produce a tetrad effect in the chondrite-normalized REE patterns. The presence of REE-bearing mineral phases such as zircon and clays in the studied deposit is likely to be a mechanism that causes the tetrad effect in the pattern distribution of REE (Rezaei Azizi et al., 2017).

Veksler et al. (2005) and Wu et al. (2011) demonstrated that superchondritic or subchondritic behavior of Y-Ho pairs and the presence of tetrad effect phenomena (convex or M-shape) may be indicative of F- and/or Si-rich immiscible melts and hydrothermal fluids during the evolution of igneous systems. Additionally, a prominent third tetrad effect (convex shape) is likely to have been produced during the interaction of F-rich hydrothermal fluids with the wall rock (Wu et al., 2011). This hypothesis supports the idea that during the alteration of andesite rock as a parent rock of the kaolin deposit, F-bearing hydrothermal fluids may well have played an important role.

The simultaneous occurrence of convex (M-shape) and concave (W-shape) tetrad effects have been reported from various environments and geochemical processes (Takahashi et al., 2002; Peretyazhko and Savina, 2010; Feng et al., 2011; Rezaei Azizi et al., 2017). These authors demonstrated that weathering under supergene conditions, hydrothermal alteration and the admixture of fluids with different origins may be responsible for the conjugate

existence of convex and concave tetrad effect phenomena in systems. According to XRD results, the presence of minerals such as goethite and hematite can be attributed to supergene activities in this kaolin deposit. Nevertheless, the concave tetrad effect of some kaolin samples reveals the low temperature meteoric nature of the fluid responsible for producing the supergene minerals such as goethite under oxidising conditions. This hypothesis is consistent with the presence of mineral phases such as illite and chlorite which are indicative of weathering conditions (Baioumy et al., 2012). Both magmatic and meteoric waters are responsible for the formation of kaolin deposits such as those in the Çanakkale Province and the kaolin deposit in Çakmaktepe, Turkey and Summitville, Colorado (Rye et al., 1992; Yıldız and Başaran, 2015; Ercan et al., 2016). Based on the aforementioned interpretations, it can be deduced that during the deposition of kaolin and evolutionary processes, both hypogene and supergene processes are likely to have played an important role in the kaolinization of andesite rocks in the studied district.

6 Conclusions

From the results of REE behavior, computed third tetrad effect values, geochemically isovalent pairs such as Y-Ho, Zr-Hf and Nb-Ta, and the correlation of these pairs with the T_3 tetrad effect in the kaolin samples of the Hizeh-Jan kaolin deposit, it can be concluded that:

(1) The frequency of the T_3 tetrad effect can be used as a geochemical indicator to distinguish the fault zone of the kaolin deposit.

(2) Field observations and correlation of Y/Ho, Nb/Ta and Zr/Hf ratios with T_3 tetrad effect values reveal a hypogene origin for this deposit.

(3) The occurrence of a negative Ce anomaly in the kaolin samples is due to the destruction of zircon by acidic oxidizing fluids.

(4) The occurrence of a negative Eu anomaly in the kaolin samples is related to the destruction of the plagioclase of the andesitic rocks by hydrothermal fluids.

(5) The occurrence of simultaneously convex and concave tetrad effect phenomena in the studied district indicates that hypogene fluids and meteoric waters under oxidising conditions are likely to have been the main probable source for kaolinization of the andesite rocks.

(6) The remarkable T_3 tetrad effects in some kaolin samples indicate that kaolinization of andesite rocks was controlled by tectonic structures.

Acknowledgments

This work was supported financially by the Research Bureau of Urmia University. The authors would like to express their thanks and gratitude to the authorities of this bureau. Our gratitude is further expressed to Prof. Degan Shu, Dr. Lian Liu, and two other anonymous reviewers for reviewing our manuscript and making critical comments and valuable suggestions, which have definitely improved the quality of this paper. Dr Fei Hongcai is thanked for assistance with English.

Manuscript received Feb. 4, 2018
accepted Jun. 2, 2018
associate EIC HAO Ziguo
edited by LISTON J. Jeffery and FEI Hongcai

References

Abedini, A., and Calagari, A.A., 2013. Rare earth elements geochemistry of Sheikh-Marut laterite deposit, NW Mahabd, West-Azarbaidjan province, Iran. *Acta Geologica Sinica* (English Edition), 87(1): 176–185.

Abedini, A., and Calagari, A.A., 2015. Geochemical characteristics of the Abgarm kaolin deposit, NW Iran. *Neues Jahrbuch für Geologie und Paläontologie – Abhandlungen*, 278: 335–350.

Abedini, A., and Calagari, A.A., 2016. Geochemical characteristics of the Arabshah kaolin deposit, Takab geothermal field, NW Iran. *Arabian Journal of Geoscience*, 9 (548): 1–16.

Abedini, A., Calagari, A.A., and Naseri, H. 2016. Mineralization and REE geochemistry of hydrothermal quartz and calcite of Helmesi vein-type copper deposite, NW Iran. *Neues Jahrbuch für Geologie und Paläontologie Abhandlungen*, 281: 123–134.

Abedini, A., Rezaei Azizi, M., Calagari, A.A., and Cheshmehsari, M., 2017. Rare earth element geochemistry and tetrad effects of the Dalir phosphatic shales, northern Iran. *Neues Jahrbuch für Geologie und Paläontologie-Abhandlungen*, 286: 169–188.

Abedini, A., Calagari, A.A., and Rezaei Azizi, M. 2018a. The tetrad-effect in rare earth elements distribution patterns of titanium-rich bauxites: Evidence from the Kanigorgeh deposit, NW Iran. *Journal of Geochemical Exploration*, 186: 129–142.

Abedini, A., Rezaei Azizi, M., and Calagari, A.A., 2018b. The lanthanide tetrad effect in argillic alteration: An example from the Jizvan district, northern Iran. *Acta Geologica Sinica* (English Edition), 92(5): 1468–1485.

Abedini, A., Rezaei Azizi, M., and Calagari, A.A., 2018c. Lanthanide tetrad effect in limestones: A tool to environment analysis of the Ruteh Formation, NW Iran. *Acta Geodynmica et Geolmaterialia*, 191(3): 229–246.

Aldanmaz, E., Pearce, J.A., Thirlwall, M.F., and Mitchell, J.G., 2000. Petrogenic evolution of Late Cenozoic, post-collisional volcanism in western Anatolia, Turkey. *Journal of Volcanology and Geothermal Research*, 102: 67–95.

Anders, E., and Grevesse, N., 1989. Abundances of the elements: Meteoritic and solar. *Geochimica et Cosmochimica Acta*, 53: 187–214.

Badanina, E.V., Syritso, L.F., Volkova, E.V., Thomas, R., and Trumbull, R.B., 2010. Composition of Li-F granite melt and its evolution during the formation of the ore-bearing Orlovka Massif in Eastern Transbaikalia. *Journal of Petrology*, 18: 131 –157.

Badel, M., Angorani, S., and Shariat Panahi, M., 2011. The application of median indicator kriging and neural network in modeling mixed population in an iron ore deposit. *Computers & Geosciences*, 37: 530–540.

Baioumy, H., 2014a. Mineralogy and *geochemistry* of clay fractions from different saprolites, Egypt: Implications for the source of sedimentary *kaolin deposits.* Russ. *Journal of Geology and Geophysics*, 55: 1367–1378.

Baioumy, H., 2014b. *Geochemistry* and origin of the Cretaceous sedimentary *kaolin deposits,* Red Sea, Egypt. *Chemie der Erde – Geochemistry,* 74: 195–203.

Baioumy, H., 2014c. Provenance of sedimentary kaolin deposits in Egypt: Evidences from the Pb, Sr and Nd isotopes. *Journal of African Earth Science*, 100: 532–540.

Baioumy, H.M., Gilg, H.A., and Taubald, H., 2012. Mineralogical and Geochemistry of the sedimentary kaolin deposits from Sinai, Egypt: Implication for control by the source rocks. *Clays and Clay Minerals*, 60: 633–654.

Ballouard, C., Poujol, M., Boulvais, P., Branquet, Y., Tartese, R., and Vigneresse, J.L., 2016. Nb-Ta fractionation in peraluminous granites: A marker of the magmatic-hydrothermal transition. *Geology*, 44: 231–234.

Bau, M., 1996. Controls on the fractionation of isovalent trace

elements in magmatic and aqueous systems: Evidence from Y/Ho, Zr/Hf, and lanthanide tetrad effect. *Contributions to Mineralogy and Petrology*, 123: 323–333.

Bau, M., and Dulski, P., 1995. Comparative study of yttrium and rare earth element behaviors in fluorine-rich hydrothermal fluids. *Contributions to Mineralogy and Petrology*, 119: 213–223.

Bolhar, R., Kamber, B.S., Moorbath, S., Fedo, C.M., and Whitehouse, M.J., 2004. Characterisation of early Archaean chemical sediments by trace element signatures. *Earth and Planetary Science Letters*, 222: 43–60.

Brindley, G.W., 1980. Quantitative x-ray analysis of clays. In: Brindley, G.W., and Brown, G. (eds.), *Crystal structures of clay minerals and their x-ray identification*. Mineralogical Society Monograph, 5, London: 411–438

Burnham, A.D. and Berry, A.J., 2014. The effect of oxygen fugacity, melt composition, temperature and pressure on the oxidation state of cerium in silicate melts. *Chemical Geology*, 366: 52–60.

Cao, M.J., Zhou, Q.F., Qin, K.Z., Tang, D.M., and Evans, N.J., 2013. The tetrad effect and geochemistry of apatite from the Altay Koktokay No. 3 pegmatite, Xinjiang, China: Implications for pegmatite petrogenesis. *Mineralogy and Petrology*, 107: 985–1005.

Censi, P., Sprovieri, M., Saiano, F., Di Geronimo, S.I., Larocca, D., and Placenti, F., 2007. The behavior of REEs in Thailand's Mae Klong estuary: Suggestions from the Y/Ho ratios and lanthanide tetrad effects. Estuarine, *Coastal and Shelf Scienc*e, 71: 569–579.

Cunha, M.C.L., Nardi, L.V.S., and Müller, I.F., 2012. Biogeochemistry of REE elements and tetrad effect in plants from volcanic soils in southernmost Brazil. *Anais da Academia Brasileira de Ciências*, 84: 911–918.

Dill, H.G., 2010. The "chessboard" classification scheme of mineral deposits: Mineralogy and geology from aluminum to zirconium. *Earth-Science Reviews*, 100: 1–420.

Dill, H.G., 2016. Kaolin: Soil, rock and ore from the mineral to the magmatic, sedimentary, and metamorphic environments. *Earth-Science Reviews*, 161: 16–129.

Dostal, J., Kontak, D.J., Gerel, O., Shellnutt, J.G., and Fayek, M., 2015. Cretaceous ongonites (topaz-bearing albite-rich microleucogranites) from Ongon Khairkhan, Central Mongolia: Products of extreme magmatic fractionation and pervasive metasomatic fluid: rock interaction. *Lithos*, 236-237: 173–189.

Ekambaram, V., Brookins, D.G., Rosenburg, P.E., Emanuel, K.M., 1986. REE geochemistry of fluorite-carbonate deposits in Western Montana, USA. *Chemical Geolgy*, 54: 319–331.

Ercan, H.U, Ece, O.I., Schroeder, P.A., and Karacik, Z., 2016. Differentiating styles of alteration within kaolin-alunite hydrothermal deposits of Canakkale, NW Turkey. *Clays and Clay Minerals*, 64: 245–274.

Feng, J.L., Gao, S.P., and Zhang, J.F., 2011. Lanthanide tetrad effect in ferromanganese concretions and terra rossa overlying dolomite during weathering. *Chemie der Erde*, 71: 349–362.

Fulignati, P., Gioncada A., and Sbrana, A., 1999. Rare earth element (REE) behaviour in the alteration facies of the active magmatic-hydrothermal system of Vulcano (Aeolian Islands, Italy). *Journal of Volcanology and Geothermal Researc*h, 88: 325–342.

Garcia-Valles, M., Pi, T., Alfonso, P., Canet, C., Martinezi, S., Jimenez-Franco, A., Tarrago, M., and Hernandez-Cruz, B., 2015. Kaolin from Acoculco (Puebla, Mexico) as raw material: Mineralogical and thermal characterization. *Clay Minerals*, 50: 405–416.

Ghorbani, M., 2013. The economic geology of Iran-Mineral deposits and natural resources. New York, Springer, 569.

Höhn, S., Frimmel, H.E., and Pašava, J., 2014. The rare earth element potential of kaolin deposits in the Bohemian Massif (Czech Republic, Austria). *Mineralium Deposita*, 49: 967–986.

Irber, W., 1999. The lanthanide tetrad effect and its correlation with K/Rb, Eu/Eu*, Sr/Eu, Y/Ho, and Zr/Hf of evolving peraluminous granite suites. *Geochimica et Cosmochimica Acta*, 63: 489–508.

Jahn, B.M., Wu, F., Capdevila, R., Martineau, F., Zhao, Z., and Wang, Y., 2001. Highly evolved juvenile granites with tetrad REE patterns: the Woduhe and Baerzhe granites from the Great Xing'an Mountains in NE China. *Lithos*, 59: 171–198.

Kadir, S., and Akbulut, A., 2009. Mineralogy, geochemistry and genesis of the Tasoluk kaolinite deposits in pre-Early Cambrian metamorphites and Neogene volcanites of Afyonkarahisar, Turkey. *Clay Minerals*, 44: 89–112.

Kadir, S., and Erkoyun, H., 2013. Genesis of the hydrothermal Karaçayır kaolinite deposit in Miocene volcanic and Palaeozoic metamorphic rocks of the Uşak-Güre Basin, western Turkey. *Turkish Journal of Earth Science*, 22: 444–468.

Kadir, S., Külah, T., Eren, M., Önalgil, N., and Gürel, A., 2014. Mineralogical and geochemical characteristics and genesis of the Güzel Yurt alunite-bearing kaolinite deposit within the late Miocene Gördeles ignimbrite, Central Anatolia, Turkey. *Clays and Clay Minerals*, 62: 477–499.

Karakaya, N., 2009. REE and HFS elements behaviour in the alteration facies of the Erenler Dağı volcanics (Konya, Turkey) and kaolinite occurrence. *Journal of Geochemical Exploration*, 101: 185–208.

Kunze, G.W., and Dixon, J.B., 1986. Pretreatment for mineralogical analysis. In: *Methods of soil analysis, Part 1, Physical and mineralogical methods*. Soil Science Society of America, Medison, Wisconsin, USA.

McLennan, S.M., 1994. Rare earth element geochemistry and the "tetrad" effect. *Geochimica et Cosmochimica Acta*, 58: 2025–2033.

Minami, M., Masuda, A., Takahashi, K., Adachi, M., and Shimizu, H., 1998. Y-Ho fractionation and lanthanide tetrad effect observed in cherts. *Geochemical Journal*, 32: 405–419.

Mondillo, N., Boni, M., Balassone, G., Spoleto, S., Stellato, F., Marino, A., Santoro, L., Spratt, J., 2015. Rare earth elements (REE)-Minerals in the Silius fluorite vein system (Sardinia, Italy). *Ore Geology Reviews*, 74: 211–224.

Monecke, T., Dulski, P., and Kempe, U., 2007. Origin of convex tetrads in rare earth element patterns of hydrothermally altered siliceous igneous rocks from the Zinnwald Sn–W deposit, Germany. *Geochimica et Cosmochimica Acta*, 71: 335–353.

Monecke, T., Kempe, U., Monecke, J., Sala, M., and Wolf, D., 2002. Tetrad effect in rare earth element distribution patterns: a method of quantification with application to rock and mineral samples from granite-related rare metal deposits. *Geochimica et Cosmochimica Acta*, 66: 1185–1196.

Moore, D.M., and Reynolds, R.C., 1989. *X-ray diffraction and the identification and analysis of clay minerals*. Oxford University Press, Oxford.

Nabavi M., 1976. An Introduction to the Geology of Iran. Tehran,Iran: Geological Survey of Iran Publication (in Persian).

Nardi, L.V.S., Formoso, M.L.L., Jarvis, K., Oliveira, L., Bastos Neto, A.C., and Fontana, E., 2012. REE, Y, Nb, U, and Th contents and tetrad effect in zircon from a magmatic-hydrothermal F-rich system of Sn-rare metalecryolite mineralized granites from the Pitinga Mine, Amazonia, Brazil. *Journal of South American Earth Sciences* , 33: 34–42.

Peppard, D.F., Mason, G.W., and Lewey, S., 1969. A tetrad effect in the liquid–liquid extraction ordering of lanthanide (III). *Journal of Inorganic and Nuclear Chemistry*, 31: 2271–2272.

Peretyazhko, I.S., and Savina, E.A., 2010. Tetrad effects in the rare earth element patterns of granitoid rocks as an indicator of fluoride silicate liquid immiscibility in magmatic systems. *Petrology*, 18: 514–543.

Rezaei Azizi, M., Abedini, A., Alipour, S., Niroomand, S., Sasmaz, A., and Talaei, B., 2017. Rare earth element geochemistry and tetrad effects in fluorites: A case study from the Qahr-Abad deposit, Iran. Neues *Jahrbuch für Geologie und Paläontologie –Abhandlungen*, 383: 255–273.

Rye, R.O., Bethke, P.M., and Wasserman, M.D., 1992. The stable isotope geochemistry of acid sulfate alteration. *Economic Geology*, 87: 225–262.

Santos, M.D.C., Varajao, A.F.D.C., and Yvon, J., 2006. Geochemistry of a sedimentary lateritic kaolin deposit in

Quadrilatero Ferrıfero, Brazil. *Journal of Geochemical Exploration*, 88: 318–320.
Schroeder, P.A., and Erickson, G., 2014. Kaolin: From ancient porcelains to nanocomposites. *Elements*, 10: 177–182.
Selmani, S., Essaidi, N., Gouny, F., Bouaziz, S., Joussein, E., Driss, A., Sdriri, A., and Rossignol, S., 2015. Physical–chemical characterization of Tunisian clays for the synthesis of geopolymers materials. *Journal of African Earth Sciences*, 103: 113–120.
Spandler, C., and Morris, C., 2016. Geology and genesis of the Toongi rare metal (Zr, Hf, Nb, Ta, Y and REE) deposit, NSW, Australia, and implications for rare metal mineralization in peralkaline igneous rocks. *Contributions to Mineralogy and Petrology*, 171: 1–24.
Stepanov, A., Mavrogenes, J.A., Meffre, S., and David Son, P., 2014. The key role of mica during igneous concentration of tantalum. *Contributions to Mineralogy and Petrology*, 167: 1009–1016.
Takahashi, Y., Yoshida, H., Sato, N., Hama, K., Yusa, Y., and Shimizu, H., 2002. W- and M-type tetrad effects in REE patterns for water–rock systems in the Tono uranium deposit, central Japan. *Chemical Geology*, 184: 311–335.
Tang, M., Wang, X.L., Shu, X.J., Wang, D., Yang, T., and Gopon, P., 2014. Hafnium isotopic heterogeneity in zircons from granitic rocks: Geochemical evaluation and modeling of "zircon effect" in crustal anatexis. *Earth and Planetary Science Letters*, 389: 188–199.
Tematio, P., Tchaptchet, W.T., Nguetnkam, J.P., Mbog, M.B., and Yongue Fouateu R., 2017. Mineralogical and geochemical characterization of weathering profiles developed on mylonites in the Fodjomekwet-Fotouni section of the Cameroon Shear Zone (CSZ), West Cameroon. *Journal of African Earth Sciences*, 131: 32–42.
Veksler, I.V., Dorfman, A.M., Kamenetsky, M., Dulski, P., and Dingwell, D., 2005. Partitioning of lanthanides and Y between immiscible silicate and fluoride melts, fluorite and cryolite and the origin of the lanthanide tetrad effect in igneous systems. *Geochimica et Cosmochimica Acta*, 69: 2847–2860.
Wang, J., Zuo, R., and Caers, J., 2017. Discovering geochemical patterns by factor-based cluster analysis. *Journal of Geochemical Exploration*, 181: 106–115.
Wu, C.Z., Liu, S.H., Gu, L.X., Zhang, Z.Z., and Lei, R.X., 2011. Formation mechanism of the lanthanide tetrad effect for a topaz and amazonite-bearing leucogranite pluton in eastern Xinjiang, NW China. *Journal of Asian Earth Sciences*, 42: 903–916.
Yıldız., A., and Başaran C., 2015. Sediment-hosted kaolin deposit from Çakmaktepe (Uşak, Turkey): Its mineralogy, geochemistry, and genesis. *Clays and Clay Minerals*, 63: 235–261.
Zaraisky, G.P., Korzhinskaya, V., and Kotova, N., 2010. Experimental studies of Ta_2O_5 and columbite-tantalite solubility in fluoride solutions from 300 to 550°C and 50 to 100 MPa. *Mineralogy and Petrology*, 99: 287–300.
Zarei, A., Malekzadeh Shafaroudi, A., and Karimpour, M.H., 2017. Geochemistry and genesis of iron‐apatite ore in the Khanlogh deposit, Eastern Cenozoic Quchan-Sabzevar Magmatic Arc, NE Iran. *Acta Geologica Sinica* (English Edition), 90(1): 121–137.
Zhao, Z.H., Xiong, X.L., Han, X.D., Wang, Y.X., Wang, Q., Bao, Z.W., and Jahn, B.M., 2002. Controls on the REE tetrad effect in granites: Evidence from the Qianlishan and Baerzhe Granites, China. *Geochemical Journal*, 36: 527–543.

About the first author

Dr. Ali ABEDINI is an associate professor of the economic geology in the Department of Geology, Faculty of Sciences, Urmia University, Iran. He is the author and co-author of 235 papers on geochemical characteristics and genesis of kaolin, bauxite, laterite, bentonite, fluorite, phosphate, limestone, claystone, epithermal, porphyry, and redbed-type copper deposits of Iran.